JOURNAL OF MATERIALS SCIENCE 26 (1991) 4076–4085

X-ray tomographic microscopy of fibre-reinforced materials

U. BONSE, R. NUSSHARDT, F. BUSCH, R. PAHL
Institute of Physics, University of Dortmund, 4600 Dortmund, Germany

J. H. KINNEY, Q. C. JOHNSON, R. A. SAROYAN
Chemistry and Materials Science, Lawrence Livermore National Laboratory, University of California, Livermore, CA 94550, USA

M. C. NICHOLS
Materials Department, Sandia National Laboratories, Livermore, CA 94550, USA

Aluminium composites containing Al_2O_3 fibres and precipitates of various intermetallic phases are investigated by high-resolution computerized microtomography. Individual fibres 15 μm in diameter and intermetallic phases forming a network with about 15 μm mesh size have been imaged. The capabilities of the method and its further development down 1 μm and less spatial resolution are discussed.

1. Introduction

Composite materials can be engineered to meet numerous specialized requirements. They can provide, for example, an unprecedented combination of high specific stiffness and strength and still have only moderate mass density. For their development, special tools are needed that allow the nondestructive analysis of internal structure.

In studies performed to understand the mechanical properties of fibre-reinforced materials, valuable information can be deduced from the correlation of measured stress and strain values with a number of internal geometrical parameters which cannot be measured at the specimen surface. Of great importance in this context are the volume fraction, nearest neighbour distance, orientation, length, and thickness of the fibres in the composite. The changes in these parameters during plastic flow, the nucleation of cracks with respect to the fibres and the growth of cracks and their topology during fracture, represent important information for successful materials engineering. Furthermore, the interaction of fibres with regions of different intermetallic phases needs to be studied. This requires an analysis of the distribution of phases within the matrix.

The recently developed X-ray tomographic microscopy (XTM) method [1–5], which is based on the use of synchrotron X-radiation (SR) in combination with an area detector, is very well suited to yield information about the internal structure of a mm-size composite sample nondestructively, and in 3-D [6]. In the past, almost any 3-D investigation requiring spatial resolution on the order of a few microns depended on repeated sectioning of the sample and on imaging each section in two dimensions by techniques like optical or scanning electron microscopy. These 2-D imaging methods are capable of providing the spatial resolution necessary for seeing precipitated intermetallic phases as well as individual fibres or freshly nucleated cracks. However, preparing the sample for 2-D microscopy quite often changes its structure and property considerably. Artifacts may be introduced or evidence may be covered up. Also, the sequence in which cracks developed cannot be obtained using post-mortem-analysis. Therefore a truly not invasive imaging method is highly desirable.

We describe here the application of XTM to the study of two Aluminium composites, one with Al_2O_3 whiskers only 2–4 μm diameter (sample 1), the other with Al_2O_3 fibres about 20 μm diameter (sample 2). As we will show below, using XTM we were able to image in sample 1 the clustering of intermetallic precipitates. In sample 2 we could even resolve the individual fibres. Furthermore, by exploiting the elemental sensitivity of XTM, we succeeded in imaging precipitates of different intermetallic phases in the composite matrix and correlated them with structures seen on optical, back-scattered electron (BSE), and wavelength dispersive (WDS) micrographs. The power of XTM as a high-resolution and nondestructive 3-D imaging method sensitive to elemental distribution, density changes, and binding state fluctuations becomes evident from our results.

2. Experimental procedure

Measurements on sample 1 were performed on the 31 pole wiggler beamline 10–2 of SPEAR at SSRL (Stanford) employing a pair of symmetrically cut (220) silicon crystals as monochromator and a Peltier-cooled CCD detector. Sample 2 was investigated on the bending-magnet beamline of the Two-Axis-Diffractometer [7] at DORIS of HASYLAB (Ham-

0022–2461/91 $03.00 + .12

burg) employing a cryogenically cooled CCD and the crystal magnifier described below. Furthermore, a special Germanium monochromator combining an asymmetrically cut (5 1 1) crystal with a symmetric (3 3 3) crystal [8] was optionally used. While preserving the nondispersive double crystal setting, the choice of the homologous reflections (5 1 1) and (3 3 3) provides different crystallographic orientations for the crystals so that the occurrence of Laue spots is minimized. The asymmetry of the first crystal increases the acceptance of radiation from the SR source and at the same time reduces the divergence of the beam incident on the sample which improves spatial resolution.

While the wiggler beamline is superior with respect to intensity, the more elaborate monochromator at DORIS allows better control of vertical beam size and divergence and of harmonic content. A monochromator optimized for XTM is expected to produce a beam with < 0.2 mrad divergence, 1 to 5 mm^2 cross section, wide energy tunability at $< 0.02\%$ bandwidth and total harmonic content less than 0.1%. Typical storage ring operation parameters were 3.3 GeV, 30 mA, 12 h lifetime at SPEAR and 3.65 GeV, 75 mA, 4 h at DORIS.

Fig. 1 illustrates the experimental arrangement used at DORIS. MC is the monochromator. SH is an additional beam shutter used in combination with an optical shutter in front of the CCD. A is the crystal magnifier, FL the fluorescent screen, and MI is an optical mirror which in combination with the objective L serves to image FL onto the CCD. SC1, SC2, and SC3 are monitor counters used in aligning MC and A. Harmonic suppression/selection is achieved by suitably detuning the component crystals of MC with respect to each other. For this to function in a proper way, the first crystal of MC is internally water-cooled [8] in order to maintain its undeformed perfect crystal state under the unavoidable heatload delivered to it by the primary beam. The energy dispersive solid state detector SSD is used for monitoring the harmonic content and for energy calibration.

The sample S is mounted on a rotary stage capable of 360 deg rotation at 0.001 degree minimum increment. Typical angular increments between individual projections varied from 0.25 to 3 deg depending on the required spatial resolution. For taking empty-beam references, the sample is shifted out of the beam in a direction parallel to its rotation axis. When the primary beam is not stationary, it is necessary to have references taken frequently. In order not to spend too much time removing the sample and setting it back, we constructed a device capable of withdrawing it at a speed > 4 cm s^{-1}. After the reference has been taken, the sample is placed back into the beam at the same speed. The original sample position is reproduced to better than 1 μm accuracy. This is an important feature in order not to deteriorate spatial resolution through uncontrolled positional changes of the sample between exposures.

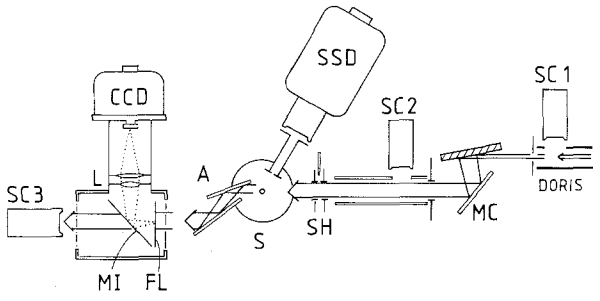

Figure 1. Experimental setup used at DORIS (Hamburg). MC: double crystal monochromator, SH: additional X-ray beam shutter, S: sample, SSD: energy dispersive solid state detector, A: X-ray optical magnifier, FL: fluorescent screen, MI: optical mirror, L: objective, CCD: cryogenically cooled Charge Coupled Detector (two-dimensional), SC1, SC2, SC3: monitor detectors used in alignment.

Presently available CCD detectors both are damaged when exposed to X-rays and become transparent at photon energies above 10 keV. Hence X-ray-to-light conversion by a fluorescent screen or by a single-crystal scintillator is necessary. The advantage in using a single-crystal is that scattering of light inside the scintillator is negligible whereas with a polycrystalline screen light scattering is an additional cause of limited spatial resolution. On the other hand, a fluorescent screen is usually 10 to 50 times more efficient than the single crystal scintillator.

The conversion of X-rays to light allows the use of straightforward optical light magnification to lessen the resolution requirements imposed on the CCD. Problems of limited spatial resolution inherent in X-ray-to-light converters are overcome by employing X-ray-optical magnification [9, 10] provided by twofold asymmetric Bragg reflection, the principle of which is explained by Fig. 2. The crystal magnifier consists of a grooved crystal with walls oriented at opposite asymmetry with respect to the reflecting Bragg planes. Fig. 3 shows a magnifying crystal which uses 2 2 0 (4 4 0) reflections with X-rays of about 9 keV (18 keV) energy, respectively. With this crystal, linear X-ray optical magnification in the range of two- to tenfold is achieved, the actual magnitude depending on the energy of the radiation used.

Two kinds of converters, a $CdWO_4$ single crystal plate 0.5 mm thick and an Eu-doped Y_2O_2S fluorescent screen about 40 μm thick have been used. While the fluorescent screen was—depending on photon energy—up to 15 times greater in fluorescence than the single crystal plate, the single crystal provided considerably better spatial resolution.

Projection of the fluorescent light image onto the CCD is achieved by employing either a single stand-

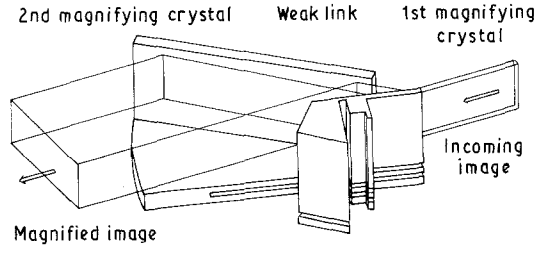

Figure 2. Function principle of the monolithic X-ray optical magnifier featuring two consecutive same-sense asymmetric Bragg reflections. The two reflecting crystal parts are connected through the weak link allowing the necessary fine adjustment.

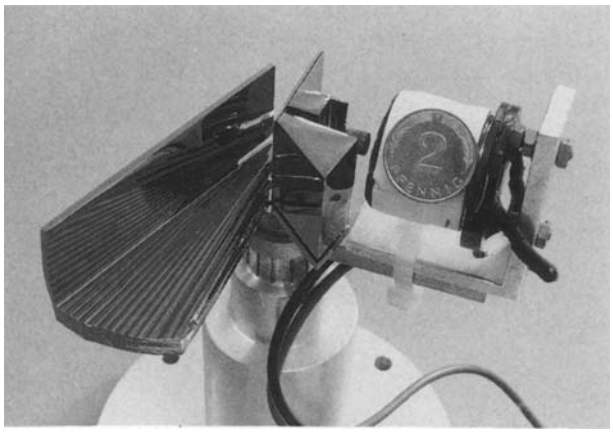

Figure 3. X-ray optical magnifier. Note the solenoid on the right and the small cylindrically shaped permanent magnet attached to the smaller Bragg reflector facing the solenoid.

ard photographic lens with 50 mm focal length or a pair of such standard lenses, one with 50 mm and the other with 120 mm focal length in telefocal geometry. With the pair of lenses, a light-optical magnification of 2.4 is obtained. With the single lens, a magnification up to about 8 is easily feasible although rarely needed. With a lens system which is custom manufactured to optimally image the screen onto the CCD, optical magnifications up to tenfold at spatial resolution of 2–3 μm can be achieved, although such resolution requires no image degradation in the scintillator screen. This is possible only below 10 keV photon energy. At higher energy the conversion of X-rays to visible light is stretched out over a depth range which is likely to exceed the depth of focus range of the lens.

Combining the X-ray optical with the light optical method of enlarging the projections, an overall magnification of up to 100 between the sample and the CCD is possible. At this magnification, to detect in the sample a detail of 1 μm size requires a CCD pixel size of less than 50 μm, which is easily obtained with commercially available CCD's. On the other hand, the maximum magnification is likely to be difficult to work with and in many cases will limit the size of the field of view unduly. These considerations, when taken together, indicate that CCD pixel sizes of the order of 5 to 20 μm are probably best for XTM, with larger formats being desirable for imaging wider fields of view. Accordingly, the CCD types shown in Table I have been employed.

The CCD with the smallest pixel size provides the highest resolution. However, with this CCD the maximum number of electrons that can be stored in a single pixel is only one fifth that for the other two CCD's. Hence the smaller pixel size implies an accordingly smaller dynamic range of about 5×10^3. This is to be compared to about 5×10^4 for the CCD's having larger pixels. Hence, whenever a high dynamic range combined with the use of small-pixel CCD's is required, multiple exposures per radiograph are unavoidable.

At SSRL data readout and processing was performed on a Microvax II and a VaxStation 3200 equipped with total CPU memory of 32 Mbyte and

Table I CCD detectors used for XTM

Type	Format	Pixel size
Thomson CSF TH7882CDA	384 × 576	23 μm × 23 μm
Texas Instruments 4849	390 × 584	22 μm × 22 μm
Kodak KAF-1400	1320 × 1035	6.8 μm × 6.8 μm

total disk space of about 3 Gbyte. A typical run for sample 1 included 365 radiographs each 736 columns wide and 421 rows high on the KAF-1400 CCD, measured at 1 degree angular increments. Slightly more than half of the radiographs were references taken of the empty beam. With the wiggler source, employing 2.4 × optical magnification and the above CCD, exposure times per radiograph ranged from 5 to 15 s, with the longer exposure related to the beam decay during the scan. Allowing also for time spent on readouts and mechanical motions of the sample, a typical run required from 2 to 5 h of beam time. Between runs, a quick reconstruction of a single slice was made for survey purposes, using reduced data sets of only 100 columns obtained by averaging. Complete data sets took roughly 20 min per reconstructed slice. All reconstructions were performed using the method of filtered back projections [11, 12].

The minimum amount of data one has to cope with in XTM may be estimated as follows. Assume a sample of width W and height H which is imaged at spatial resolution Δ. We shall require that the spatial resolution of the 3-D reconstruction is also Δ. This requirement determines the number, N, and size (R rows times C columns) of the radiographs to be collected. The size is H/Δ rows (each corresponding to one reconstruction slice in the 3-D output image) and W/Δ columns (each representing the sums of the absorption along paths through the sample at a given distance from the rotation axis). We must take $N = \pi C/4$ such radiographs at angular increments of $180/N$ deg. The resulting data contains $N \times R \times C$ voxels which require a minimum of $N \times R \times C \times B$ bytes of storage if B bytes are used to store each voxel. In practice, 20 to 100% more data is collected because of the need to collect reference and dark images in order to compensate beam instability, CCD background and CCD nonuniform pixel sensitivity. Each reconstruction slice uses at least N·C·B bytes of raw data to produce $4C^2$ bytes of real-valued output. Performing reconstructions for the entire 3-D volume produces $4R \times C^2$ bytes to be dealt with during 3-D rendering.

As an example, consider a cylindrical sample of 1 mm in diameter and 0.5 mm high which is imaged at 3 μm spatial resolution. Each radiograph will have 167 rows and 333 columns. We must take 262 radiographs with the sample rotated 0.7 deg between each exposure. The resulting data consists of about 1.5×10^7 voxels. Assuming the use of the KAF-1400 CCD which collects 12 bits of data (a dynamic range of about 4×10^3) stored in 2 bytes of memory, about 30 Mbytes of data must be stored. Each reconstruction slice uses about 174 kbytes of input to produce about 444 kbytes of output. Reconstruction of all the

data produces about 74 Mbytes of output to be rendered into a 3-D image.

Fortunately, the assumed definition of resolution reflects a very conservative point of view. It should not be confused with the detectability of smallest-size objects. It was found in practice, that objects considerably smaller than the defined resolution limit are detectable under conditions of good contrast. The correct treatment of resolution must be based on the concept of modulation transfer function (MTF) [13] which correctly accounts for the inherent link between the smallest size of a detectable object and its contrast.

It may also be pointed out that the amount of data to be measured and handled does not primarily depend on the spatial resolution but rather more simply on the number of voxels which must be examined together with what dynamic range is required in the final image. On the other hand, given a fixed sample volume, the amount of data to be measured scales with the third power of $1/\varepsilon$, ε being the smallest distance to be resolved. Hence when going to higher resolutions it becomes more important to limit the sample volume to its absolute minimum. At the same time, especially when employing CCD's with smaller and hence many more pixels, it appears very important to develop faster on-chip readout techniques and to provide storage media of several tens of Gb capacity. For fast rendering of the reconstructed 3-D image, the data of all pixels have to reside in CPU memory. This means the size of the memory should be on the order of 80 Mb and more.

3. Results

In the following discussion of the XTM images of sample 1, we will refer to 'cuts' and 'slices' as illustrated in Fig. 4. As is seen, *all* voxels of a given *slice* are related to each other through the *same* reconstruction calculation. Voxels of different slices are completely independent from each other. In contrast to this, voxels of a given *cut* are reconstruction-related only if they belong to the same *line*, where line means a line normal to the rotation axis. It is important to keep these relationships in mind when discussing the possibility that artifacts are generated by the reconstruction algorithm.

Fig. 5 shows the XTM image of slice S47 of sample 1 (Fig. 4) taken at 20 keV. The almost cylindrical shape of the sample is recognizable. Bright areas in the picture correspond to higher absorption caused by alloy-phases in the Al matrix. The phases contain elements with z-values larger than that of Al.

At first sight, the regions of strong absorption seen in Fig. 5 appear to form a three-dimensional network with an average mesh size of roughly 150 μm. However, there is another net, less absorbing than the first one, and featuring a much smaller mesh size of about 15 μm. From a closer inspection of Fig. 5 we find that the strongly absorbing regions are just clusters of meshes of smaller cell size, i.e. there is only the smaller net which, however, has nonuniform density. (Circles around the centre of rotation seen at the lower left are artefacts due to defective pixels.)

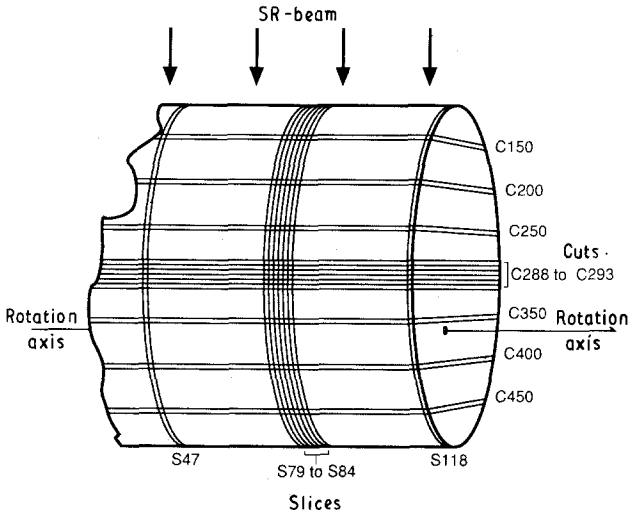

Figure 4. Identification of XTM images, which are called slices (S) if oriented at right angle, and cuts (C) if oriented parallel to the rotation axis. Numbers refer to the XTM images shown in Figs 5, 6, 9, and 10.

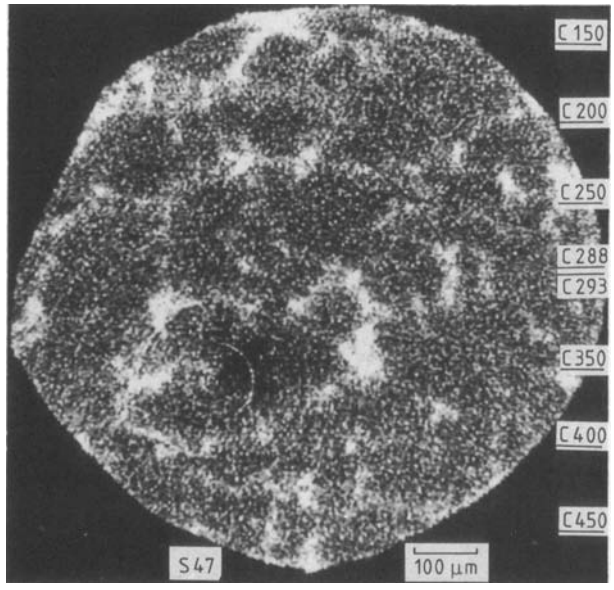

Figure 5. XTM-slice S47 (Fig. 4) taken at 20 kV of sample 1 which is an Al-composite reinforced by Al_2O_3 fibres 2 to 4 μm in diameter and 50 to 80 μm in length. Brighter areas represent increased absorption due to the presence of higher z-elements contained in alloy phases embedded in the Al matrix. The alloy phases form a network with a mesh size of about 15 μm, which seems to cluster in the very bright regions, that have an average distance of about 150 μm from each other, and possibly form another, much coarser network. At the right side the position of the cuts shown in Fig. 6 are indicated. (The concentric circles at the lower left are artefacts due to defective pixels of the CCD.)

Fig. 6 shows cuts C150, C200, C250, C350, C400, and C450, all taken at right angles to Fig. 5. The locations where these cuts have been made are indicated in Fig. 4 and also on the right side of Fig. 5 in order to see easily the correspondence of the top lines of each cut with the structure seen in Fig. 5. Evidently the structure is the same in both directions, meaning that the network has no noticeable texture.

The aluminium matrix is type KS 1275 AlSi12CuMgNi from Kolbenschmidt AG, Neckarsulm. Its stated overall composition is 11 to 13% Si, 0.8 to 1.5%

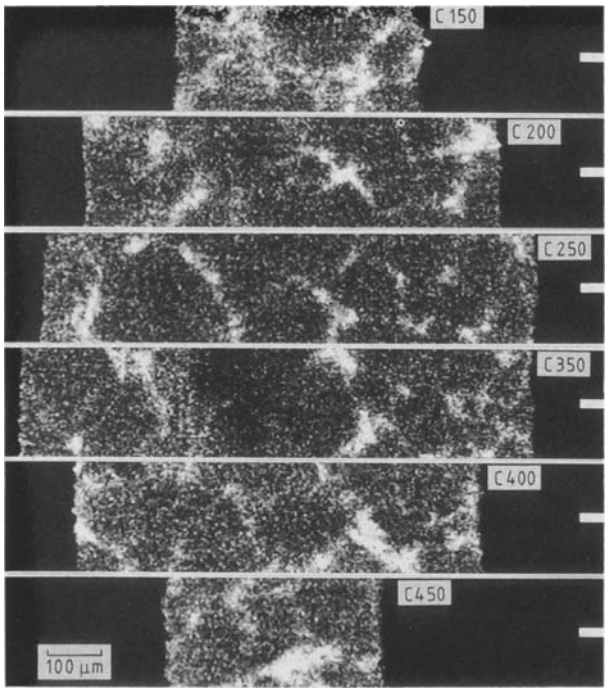

Figure 6. XTM cuts C150 to C450 of sample 1. Cuts are oriented as illustrated in Fig. 4, i.e. at right angle to the slice of Fig. 5. Note the likeness of structures seen in Figs 5 and 6. The white bars on the right denote the location of the set of neighbouring slices shown in Fig. 9.

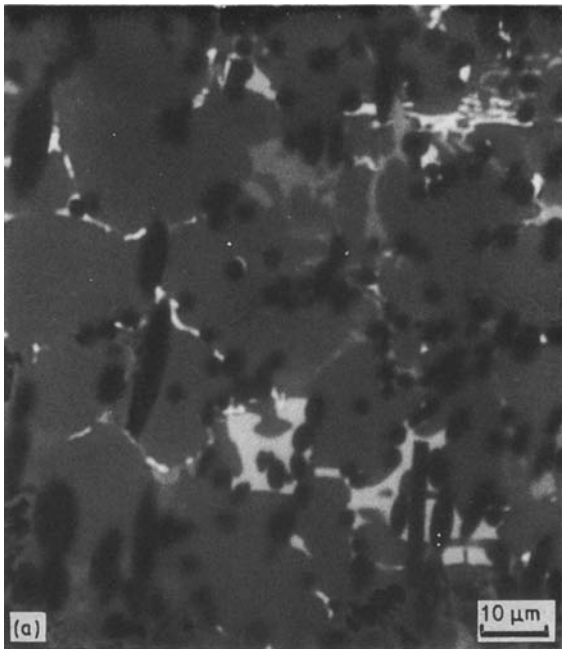

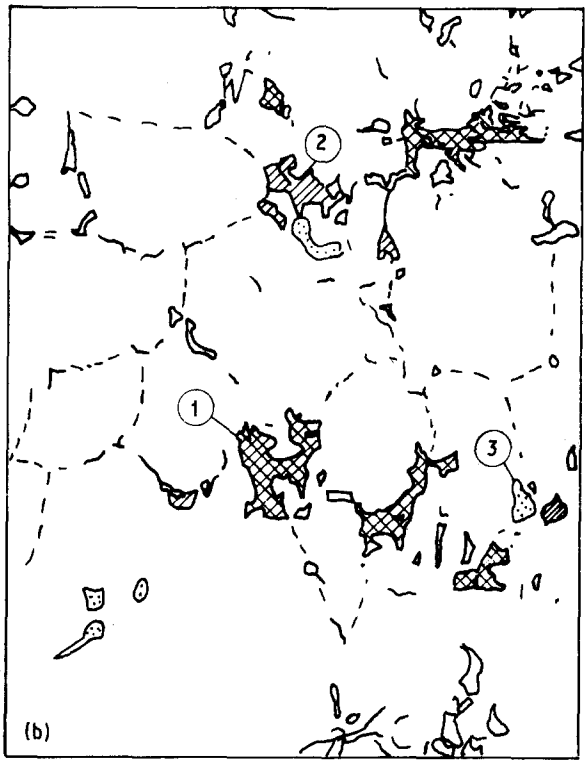

Figure 7. Identification of alloy phases in sample 1. a: BSE-map showing three different types of phases, 1 (right), 2 (grey), 3 (dark grey). b: contours of different phases and their numbering. Note that in a the phases link up to form a network with mesh size on the order of 15 µm.

Cu, < 1.3% Ni, < 0.7% Fe, < 0.2% Ti, < 0.3% Mn, < 0.3% Zn, and the balance Al. The material is normally used for pistons of diesel engines. The fibre reinforcement improves the material strength at higher working temperatures.

The elements present in the alloy phases have been identified by inspection of back-scattered electron-micrographs (BSE) and wavelength-dispersive spectrometer-maps (WDS), examples of which are shown in Figs 7 and 8. On the BSE micrograph Fig. 7a there are three types of phases distinguished, 'light', 'grey', and 'dark grey', respectively. The different types are labelled 1, 2, and 3 in Fig. 7b in which the pertinent contours of Fig. 7a have been redrawn in order to facilitate the recognition of the different phase types. From WDS-maps like those shown in Fig. 8b, c, and d for Fe, Si, and O, respectively, and other WDS-maps including Ni and Mg, it is found that phase 1 (light) contains Ni, Fe, Si, and Cu. Phase 2 (grey) contains Si, Mg, Ni, Fe, and Cu. Phase 3 (dark grey) is made up mostly of Si. Furthermore, strong evidence is obtained from the BSE-micrographs and WDS-maps that all three phases interconnect to form a three-dimensional network with an average mesh size of about 15 µm. This could correspond to the smaller net observed on the XTM micrographs Figs 5, 6, 9, and 10.

The Al_2O_3 fibres are seen as black spots on the BSE-micrographs in Figs 7a and 8a. They match perfectly with light spots on the Oxygen WDS-map shown in Fig. 8d. The fibres are also clearly seen in the optical micrograph of Fig. 11. Most Al_2O_3 fibres are oriented normal to the plane of Fig. 11. The result of a determination of all the compositions, i.e. of the matrix, of the phases 1, 2, 3, and of the fibres performed by X-ray fluorescent analysis (XFA) is given in Table II. Because of the smallness of the phase grains the amount of Al is overstated in Table II.

Al-rich alloy systems including the elements listed in Table II, i.e. Mg, Si, Fe, Ni, and Cu, are known [14] to contain the intermetallic phases shown in Table III. From the known structure of these phases we have calculated their densities as listed in column 3 of Table III. Using the elemental mass adsorption coefficients in [16], we determined the linear and relative

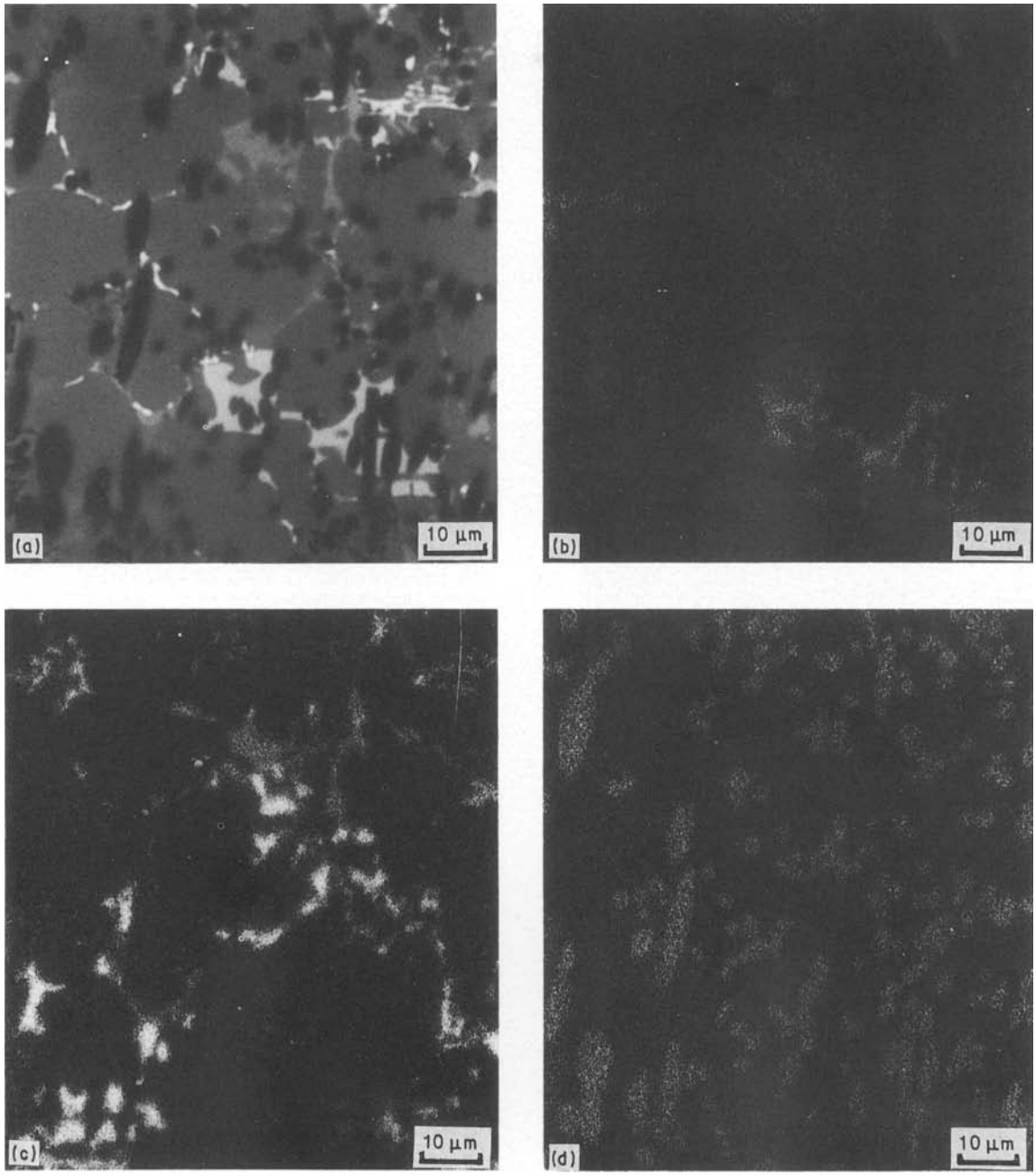

Figure 8. Identification of alloy phases in sample 1: (a) BSE-map as Fig. 7a, (b) Fe-WDS-map, (c) Si-WDS-map and (d) O-WDS-map. Note correspondence of different phases with contours in WDS-maps. The shapes of Al_2O_3 fibres in a match light region in (d).

adsorption coefficients of all components (columns 4 and 5 of Table III). Because of the low solubility of Si in Al and the presence of a considerable amount of Mg, most of the Si is present in the component Mg_2Si. Since there is not enough Mg to bind all of the Si, the rest is found as a separate component consisting of the element Si, which we believe is identical with our phase 3 seen in Fig. 7 and Fig. 8c. Considering the composition of phase 2 we find that it is very likely made up of Mg_2Si plus Al_3Ni and a small fraction of $Al_{3.2}Fe$. Similarly, we conclude that phase 1 consists of the last four components listed in Table III. The important point is that, according to the values found in Table III, the absorption is high for phase 1, medium for phase 2 and not much different from that of the Al matrix in the case of phase 3. Therefore, in XTM micrographs we expect to see essentially three main levels of contrast. This is in agreement with the observation if we interpret the bright regions to be mostly phase 1 and the less bright net structure to consist of phase 2. Because of its low contrast, phase 3 is not likely to be seen at all at these size scales.

In order to illustrate the structure of phases in three dimensions further, we show in Fig. 9 a set of six neighbouring slices (S79 to S84) and in Fig. 10 a set of six neighbouring cuts (C288 to C293) of sample 1. The distance between the mid planes of the neighbouring slices (cuts) is about 2.8 µm. This value is the resolution as defined in section 2. For sample 1 it is given by the CCD pixel size (6.8 µm) divided by the light optical magnification used (2.4). As is seen, the network structures change continuously when passing through the stack of neighbouring XTM micrographs. Taking Figs 5, 6, 9, and 10 together, it becomes evident that the structures seen are a network consisting of intermetallic phases which extend in three dimensions, and

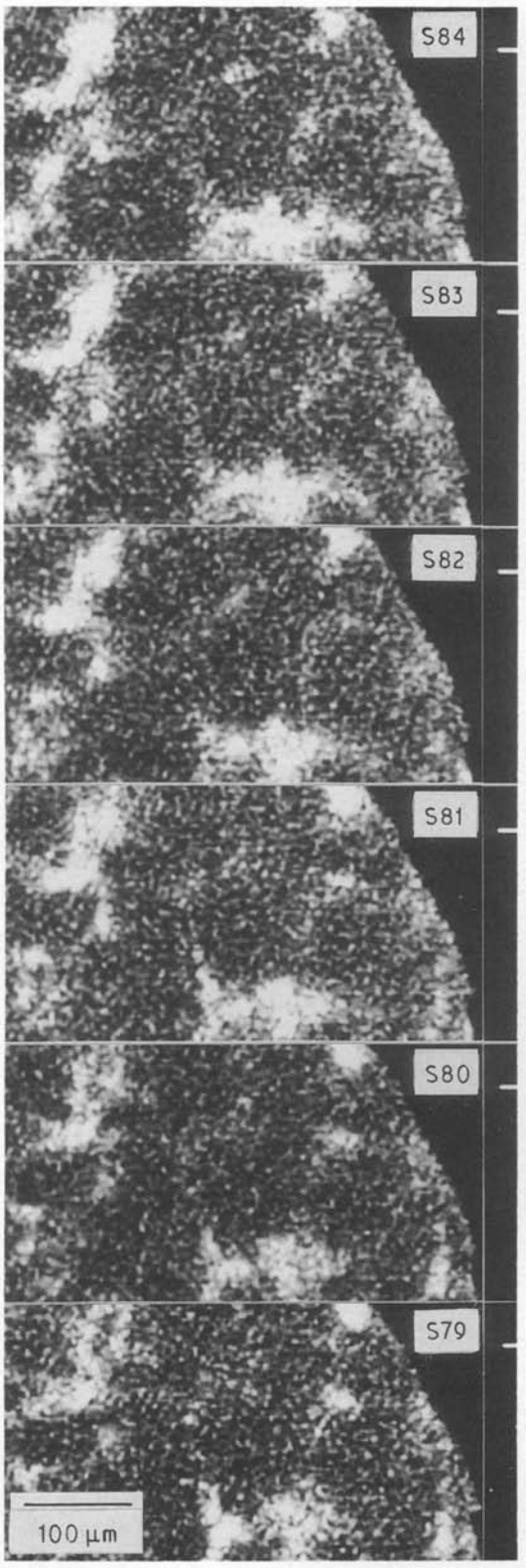

Figure 9. Set of six neighbouring XTM-slices S79 to S84 (Fig. 4) illustrating the continuity of the network between slices. The thickness of slices is about 2.8 µm. The white line on the right indicates the location of cut C200 shown in Fig. 6.

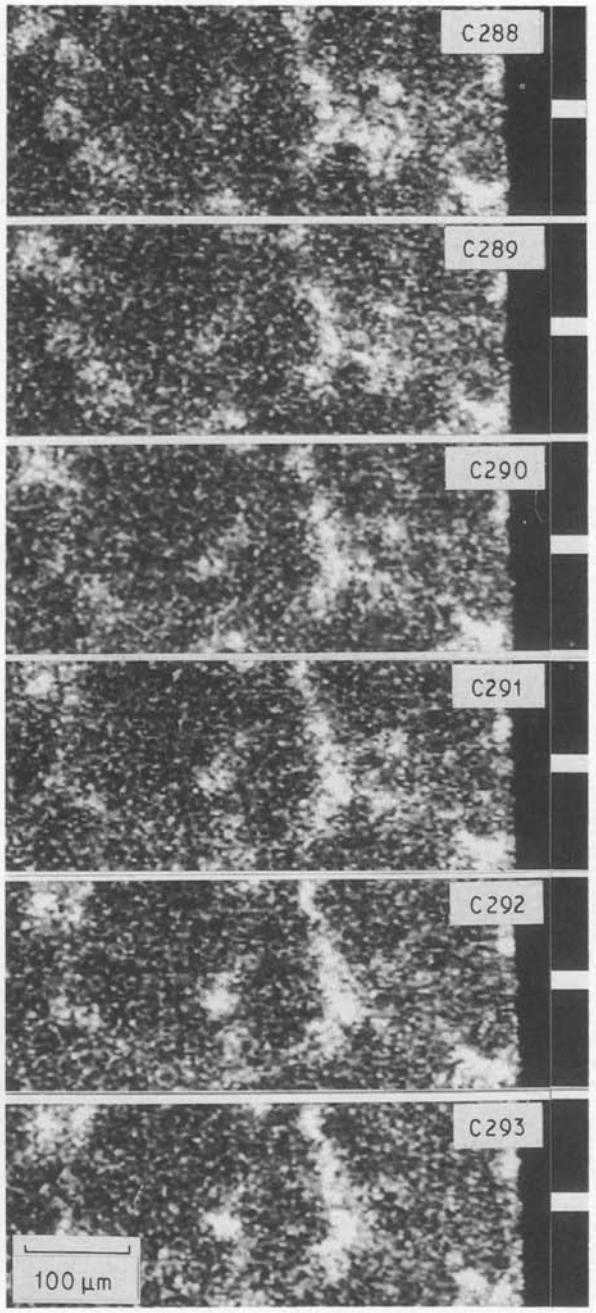

Figure 10. As Fig. 9, however the cuts C288 to C293 (Fig. 4) are shown. The white bars on the right denote the location of the set of neighbouring slices shown in Fig. 9.

which have a mesh size of the order of 15 µm. We believe this is the first time such fine and interconnected structures have been visualized nondestructively and in 3-D.

Fig. 12a is a XTM microgpaph of sample 2 taken normal to its rotation axis by employing the Thomson CSF TH7882CDA CCD combined with an X-ray optical magnification of 5.8 and a light optical magnification of 2.04. Since, in sample 2, all fibres are oriented normal to the image plane, we interpret the dark dots as cuts through individual fibres. The fibre diameter of 15–20 µm as well as the distribution of fibres is in agreement with the scanning electron micrograph Fig. 12b and also Fig. 13, which shows a single fibre at even higher spatial resolution.

The resolution of the XTM picture, Fig. 12a, when calculated simply from the CCD pixel size (23 µm) and the overall magnification ($\times 11.8$), should be $23/11.8 \approx 2$ µm. The modulation transfer function (MTF) measured for this imaging system [8] yields 80 line pairs mm^{-1} at 20% contrast, corresponding to about 6 µm resolution. This is not far from what one would estimate just by looking at Fig. 12a. Furthermore, we should point out that the MTF accounts for

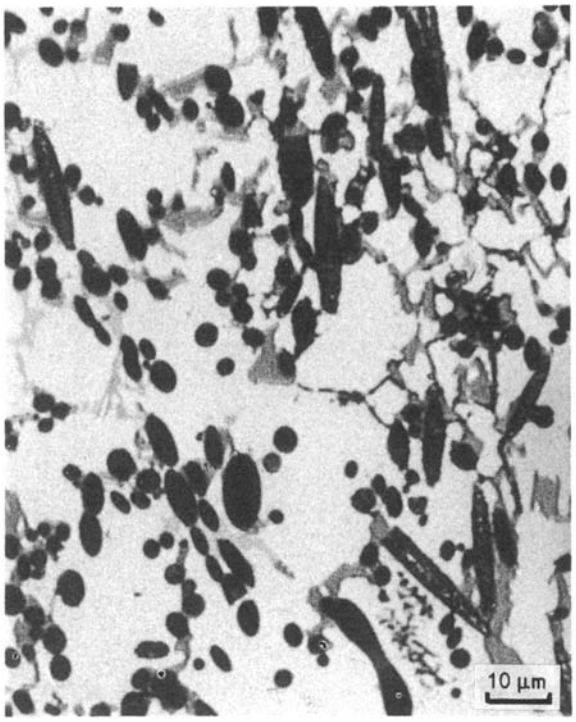

Figure 11. Optical micrograph of the surface of sample 1. The fibres are predominantly oriented normal to the image plane. The network of phases referred to in Fig. 7 can also faintly be seen.

the resolution with respect to directions parallel to the reconstructed slices, i.e. normal to the axis about which the sample is rotated (Figs 1 and 4) when the projections are measured. At right angles to this plane, i.e. parallel to the rotation axis, there is no X-ray optical magnification, which means that the resolution in this direction is expected to be poorer by a factor of 5.8. Hence the image is integrated normal to the image plane over a depth of roughly 12 µm which accounts for an additional loss of resolution. It could be avoided by placing behind A in Fig. 1 a second crystal magnifier, diffracting at right angle with respect to the first one. With the second magnifier in the beam we estimate the intensity to drop by an order of magnitude.

A single magnifying crystal, diffracting in a plane *perpendicular* to the axis of sample rotation, although directly enlarging each projection only in *one* dimension, causes the reconstructed image to become magnified in two dimensions. When the projections are measured, a very large number of *one-dimensional* magnifications of sample projections in *different directions* are made. The reconstruction algorithm transforms the *multi-directional one-dimensional* magnifications of projections into the *two-dimensionally* magnified final image. Hence, a kind of 'balance' between the amount of measured information and the amount of information contained in the reconstructed image is maintained. On the other hand, a crystal magnifier which is diffracting in a plane *parallel* to the sample's rotation axis, yields only a *one-dimensional* magnification of the reconstructed image.

The observations also confirm our theoretical estimates of resolution for the case when X-ray optical magnification is employed. Moreover, from the foregoing, we obtain substantial support for our thesis that by combining the techniques of magnification with the high resolution CCD and using a wiggler SR source, it will be possible to really achieve 3-D resolution on the scale of 1 µm and better for the XTM system.

4. Conclusion

We have demonstrated the development of XTM which has beome a valuable tool for the nondestruct-

Table II Approximate composition of sample 1 in weight per cent (wt %) and atomic per cent (at %) as determined by electron microprobe analysis.

Element	Matrix		Light Ph.		Grey Ph.		Dark Ph.		Fibre	
	(wt %)	(at %)	(wt %)	(at %)	(wt %)	(at %)	(wt %)	(at %)	(wt %)	(at %)
Oxygen	–	–	–	–	–	–	–	–	43	56
Magnesium	0.3	0.4	–	–	19.3	23	0.3	0.4	–	–
Aluminium	98	98	64	78	42	44	31	32	55	42
Silicon	1.6	1.5	1.7	2.0	27	27	68	67	1.9	1.4
Iron	–	–	7.5	4.4	2.1	1.1	–	–	–	–
Nickel	–	–	25.6	14.4	8.5	4.0	–	–	–	–
Copper	–	–	1.0	0.6	1.1	0.5	–	–	–	–

Table III Properties of components of Al-rich alloy systems containing Mg, Al, Si, Fe, Ni, and Cu.

Component [14]	Structure [15]	Density ($g\,cm^{-3}$)	Absorption 20 keV (cm^{-1})	relat.	Occurrence Phase 1	2	3
Al		2.70	9.11	1			
Si	CF8	2.33	10.15	1.11			×
Mg_2Si	CF12	2.00	6.56	0.72		×	
$Al_{3.2}Fe$	mC102	3.81	46.30	5.08	×	×	
Al_3Ni	oP16	3.98	61.88	6.79	×	×	
Al_3Ni_2	hP5	4.76	97.65	10.72	×		
Al_2Cu	tI12	4.36	86.59	9.50	×		

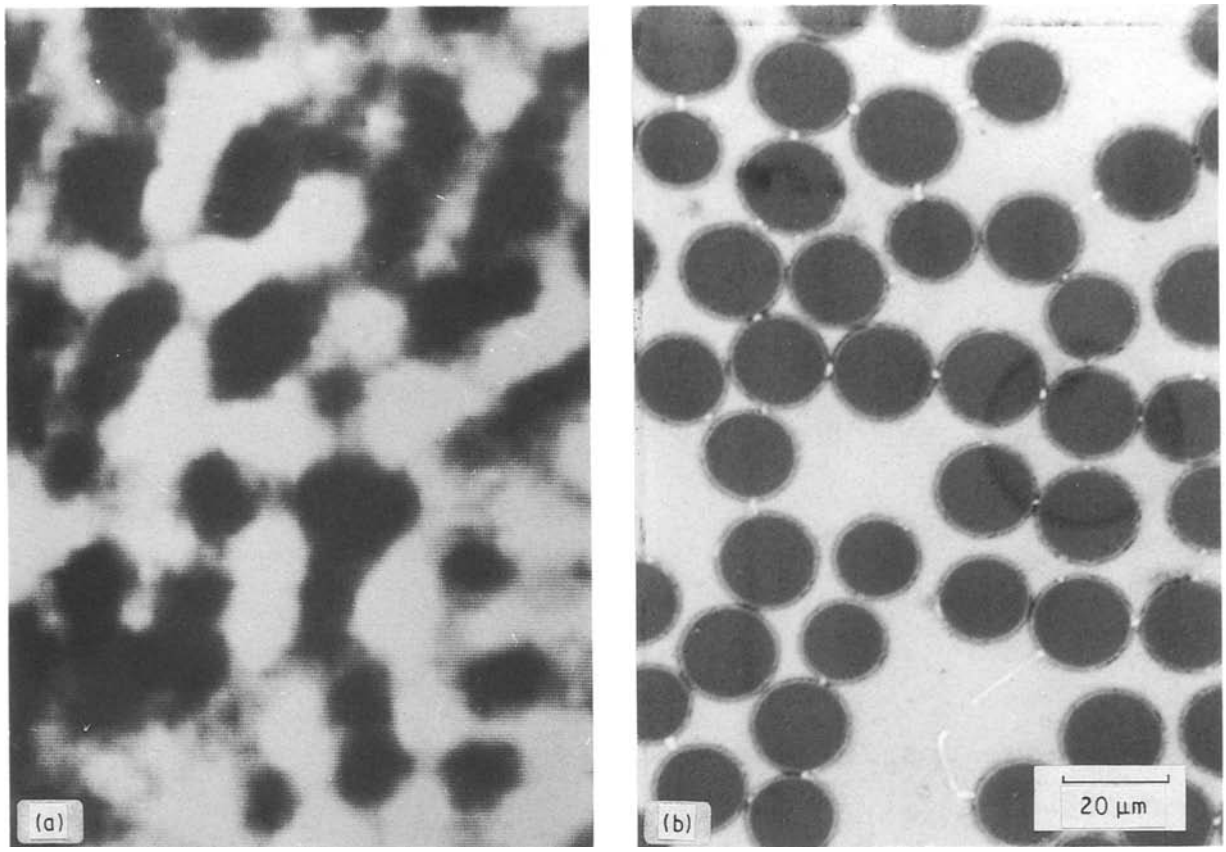

Figure 12 (a) XTM micrograph of sample 2, orientation normal to the rotation axes. (b) BSE-map of sample 2. Note the correspondence of the fibres' diameter and general distribution on either picture.

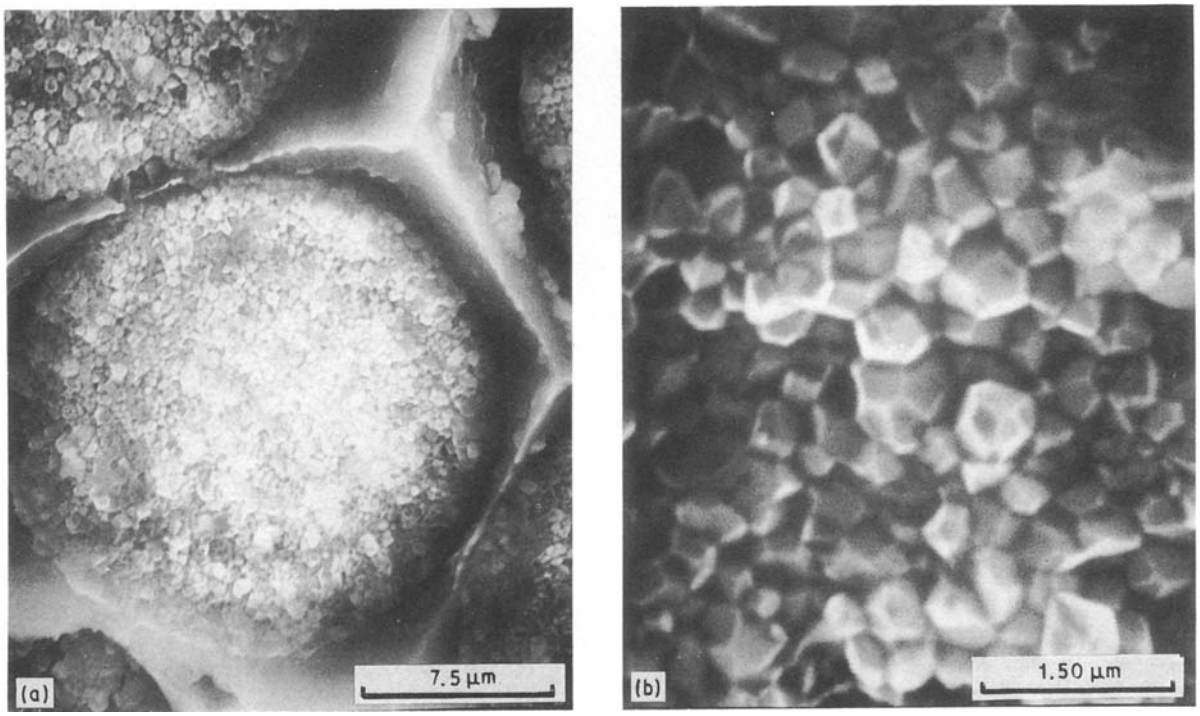

Figure 13. BSE-maps of fibres of sample 2 at larger magnification. (a) single fibre. (b) crystalline structure seen within a single fibre.

ive and three-dimensional study of Al–Al_2O_3 composites. Furthermore, its successful application for the visualization of structures of intermetallic phases has been shown. The essential components for optimized XTM are:

1. a powerful wiggler-SR source;
2. a double crystal monochromator making effective use of perfect crystal optics to suppress or select harmonics and to provide a highly parallel and monoenergetic beam;

3. a rotation and translation stage allowing rapid and reproducible incremental rotations and translations of the sample with high precision;
4. a perfect-crystal X-ray-optical magnifier;
5. a high-density high-efficiency fluorescent single crystal for converting X-rays to optical light;
6. an optimized light-optical imaging system; and
7. a high-resolution CCD detector linked to a computing system capable of fast data readout and of reconstructions of images consisting of 10^7 to 10^8 voxels.

In this study, by combining only 1, 3, 5 and 7 (above), we were able to image three-dimensional networks of intermetallic phases with mesh sizes as small as 15 μm. On the other hand, by combining only 2, 3, and 4, together with a CCD of 23 μm pixel size, we were able to see individual Al_2O_3 fibres with less than 15 μm diameter in an Al–Al_2O_3 composite material.

When all the components (listed 1 to 7) are combined, a spatial resolution on the order of 1 μm and below can be obtained. A 3-D imaging method, which is nondestructive and at the same time sensitive to elemental composition and chemical state, having this spatial resolution should be of great value in various fields of solid state research and development.

Acknowledgements

This work was supported by the Bundesminister Für Forschung und Technologie (Bonn, West Germany) under contract 03-B01DOR, and by the Department of Energy (Washington, DC, USA) under contracts W-7405 and AT-(29–1)-789. Thanks are due to C. Reimers, Quality Control, University of Dortmund, for providing samples. The authors would also like to thank the staffs of HASYLAB (Hamburg) and SSRL (Stanford) for their contributions to the smooth running of the synchrotron radiation beamlines, W. N. Massey for electronics engineering support, and A. Grohs, A. Gardea, and J. Scolla for providing optical and microprobe pictures of the samples.

References

1. U. BONSE, Q. C. JOHNSON, M. C. NICHOLS, R. NUSSHARDT, S. KRASNICKI and J. H. KINNEY, *Nucl. Instr. Meth. Phys. Res.* **A246** (1986) 644.
2. J. H. KINNEY, Q. C. JOHNSON, U. BONSE, R. NUSSHARDT, and M. C. NICHOLS, *Proc. Photo-Opt. Instrum. Eng.* **691** (1986) 43.
3. J. H. KINNEY, Q. C. JOHNSON, R. A. SAROYAN, M. C. NICHOLS, U. BONSE, R. NUSSHARDT, and R. PAHL, *Rev. Sci. Instrum.* **59** (1988), 196.
4. T. HIRANO, K. USAMI, and K. SAKAMOTO, *Rev. Sci. Instrum.* **60** (7) (1989) 2482.
5. B. P. FLANNERY, H. D. DECKMAN, W. G. ROBERGE, and K. L. D'AMICO, *Science* **237** (1987) 1439.
6. J. H. KINNEY, S R. STOCK, M. C. NICHOLS, U. BONSE, T. M. BREUNIG, R. A. SAROYOAN, R. NUSSHARDT, Q. C. JOHNSON, F. BUSCH, S. D. ANTONLOWITCH, *J. Mater. Res.*, **5** (1990) 1123.
7. U. BONSE and K. FISCHER, *Nucl. Instr. Meth.* **190** (1981) 593.
8. U. BONSE, R. NUSSHARDT, R. PAHL, Q. C. JOHNSON, J. H. KINNEY, R. A. SAROYAN, and M. C. NICHOLS, "HASYLAB Jahresbericht" (DESY, Hamburg, 1986), p. 395.
9. U. BONSE, R. NUSSHARDT, F. BUSCH, R PAHL, Q. C. JOHNSON, J. H. KINNEY, R. A. SAROYAN, and M. C. NICHOLS, *ibid* (DESY, Hamburg, 1988) p. 469.
10. U. BONSE, F. BUSCH, R. NUSSHARDT, R. PAHL, J. H. KINNEY, Q. C. JOHNSON, R. A. SAROYAN, and M. C. NICHOLS, *ibid* (DESY, Hamburg, 1989), p. 557.
11. G. T. HERMAN, "Image Reconstruction from Projections: The Fundamentals of Computerized Tomography" (Academic Press, New York, 1980).
12. R. H. HUESMAN, G. T. GULLBERG, W. L. GREENBERG, and T. F. BULDINGER, "Donner Algorithms for Reconstruction Tomography", (Lawrence Berkeley Laboratory, University of California, October 1977).
13. R. K. SWANK, *Appl. Opt.* **12** (1973), 1865.
14. "Equilibrium Diagrams of Aluminium Alloy Systems", The Aluminium Development Association, 33 Grosvenor Street, London W1, UK (The Kynoch Press, Birmingham, 1961).
15. P. VILLARS and L. D. CALVERT, "Pearson's Handbook of Crystallographic Data for Intermetallic Phases", Vol. 1 (American Society for Metals, Metals Park, OH 44073, 1985.
16. E. F. PLECHATY, D. E. CULLEN, R. J. HOWERTON, "Tables and Graphs of Photon Interaction Cross Sections from 0.1 keV to 100 MeV derived from the LLNL Evaluated Nuclear Data Library", Vol. 6 (UCRL–50400, 1981) Rev. 3.

Received 6 July
and accepted 29 October 1990